Earth and Planetary Science Letters 391 (2014) 183–192

Contents lists available at ScienceDirect

Earth and Planetary Science Letters

www.elsevier.com/locate/epsl

Plume-induced crustal convection: 3D thermomechanical model and implications for the origin of novae and coronae on Venus

T.V. Gerya

Institute of Geophysics, ETH Zürich, Sonneggstrasse 5, 8092 Zürich, Switzerland

ARTICLE INFO

Article history:
Received 9 July 2013
Received in revised form 15 January 2014
Accepted 3 February 2014
Available online 19 February 2014
Editor: C. Sotin

Keywords:
novae
coronae
plume–lithosphere interaction
thin Venus lithosphere
thermomechanical model

ABSTRACT

Novae and coronae are large volcanotectonic features on Venus, with a contentious and possibly non-unique origin and enigmatic relationship. Their formation is most commonly explained by flexure and fracturing of the strong rigid Venus lithosphere atop mantle upwelling and/or downwelling. Here we present new 3D high-resolution thermomechanical model of mantle plume/diapir impingement into warm and thin lithosphere with Venus-like surface temperature. Numerical results suggests that nova-like and corona-like structures can result from magma-assisted convection of weak ductile crust, induced by decompression melting of the hot rising mantle plume. During the initial stage, nova forms by stellate fracturing of a topographic rise forming atop the growing crustal convection cell. Few million years later, nova can convert to coronae by inward dipping concentric fracturing of the nova rise margins and subsequent outward thrusting of partially molten crustal rocks over the surface. An outer annulus of concentric normal faults forms in the outer rise region of the downbending brittle upper crust, whereas an inner annulus of concentric thrust faults forms in front of the outward thrusting crustal wedge. A trench-like depression forms between these two annuli. Resembling retreating subduction, the rudimentary concentric upper-crustal slab warms up rapidly and recycles into the convection cell. The convection cell remains active for up to 15 million years, fueled by heat and magma from the plume. Predicted surface topography and fracturing patterns agree with some small to moderate size novae and coronae on Venus.

1. Introduction

Venus novae are “radially fractured centers” 100–300 km in diameter; 64 have been identified (Crumpler et al., 1996; Aittola and Kostama, 2000; Krassilnikov and Head, 2003). These structures were also coined as “radial corona-like features” (Stofan et al., 1992) and “failed coronae” (Janes and Turtle, 1996). Dense radial fracturing and raised topography are common, and massive amounts of volcanism are seen in some. In contrast to volcanoes, novae show a dominance of tectonic activity over volcanic activity (Krassilnikov and Head, 2003). Radial fracturing patterns of novae form at early stages and associate with dike swarm emplacement (Grosfils and Head, 1995, 1996; Ernst et al., 2001), whereas concentric tectonic features (where present) are formed later (Krassilnikov and Head, 2003). Novae are subdivided into four topographic classes: (N1) upraised, (N2) annular, (N3) flat and negative, and (N4) plateau-like. 40.3% of the novae population started to form before emplacement of regional plains with wrinkle ridges on Venus and 11.3% completed their activity before this time; 88.7% of the population of novae were active after regional plains formation (Krassilnikov and Head, 2003). Detailed structural analysis shows novae evolution often but not always leading to the formation of corona-like features (Krassilnikov and Head, 2003).

Venus coronae are 513 approximately circular structures that range in diameter from 60 km to over 1000 km (Barsukov et al., 1984; Stofan et al., 1992, 2001; Glaze et al., 2002; Grindrod and Hoogenboom, 2006). Nearly all coronae have associated volcanic and tectonic features, including large numbers of small (<50 km diameter) volcanoes, extensive flow deposits, radial and concentric fractures and ridges (Squyres et al., 1992; Stofan et al., 1992, 2001; Roberts and Head, 1993). Coronae typically have a raised rim superimposed on which is an annulus of closely spaced concentric fractures and/or ridges. Based on the extent of their annulus coronae are subdivided into Type 1 (406 coronae with >180° annulus) and Type 2 (107 coronae with <180° annulus) (Stofan et al., 2001; Glaze et al., 2002). Nine topographic groups of coronae comprise (Smrekar and Stofan, 1997; Glaze et al., 2002): (C1) dome, (C2) plateau, (C3) rim surrounding interior high or dome, (C4) rim surrounding depression, (C5) outer rise, trough, rim, inner high,

E-mail address: taras.gerya@erdw.ethz.ch.

http://dx.doi.org/10.1016/j.epsl.2014.02.005
0012-821X/

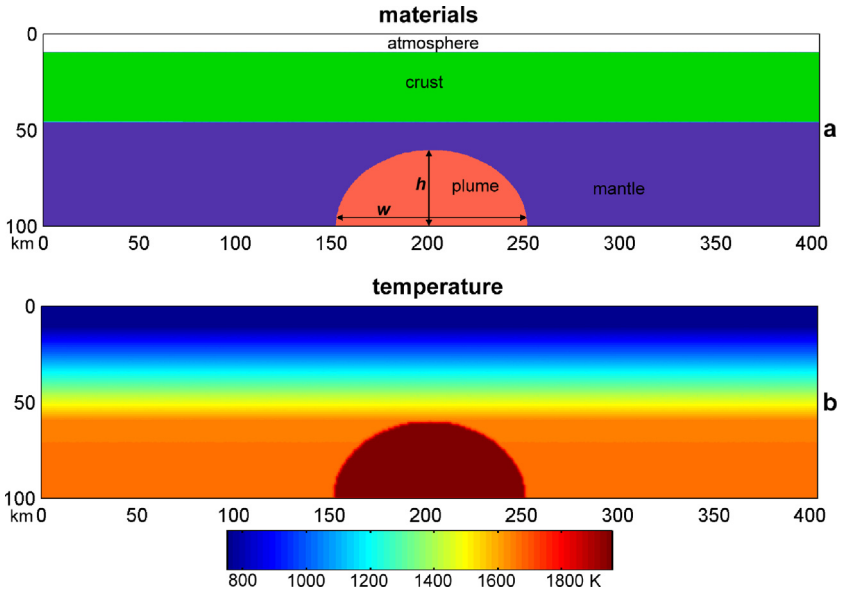

Fig. 1. Initial geometry (a) and thermal structure (b) of the numerical model. Cross-section trough the center of the model is shown. w and h are width and height of the plume/diapir, respectively (Table 1).

(C6) outer rise, trough, rim, inner low, (C7) rim only, (C8) depression, and (C9) no discernible signature. In contrast to novae, coronae activity was greatest before formation of regional plains with wrinkle ridges (Basilevsky and Head, 1998; Ivanov and Head, 2001).

Origin of novae and coronae is contentious and possibly non-unique (cf. reviews in Aittola and Kostama, 2000; Krassilnikov and Head, 2003; Grindrod and Hoogenboom, 2006). The most common explanation suggests an interaction of the strong rigid Venus lithosphere with mantle upwelling and/or downwelling (cf. reviews in Krassilnikov and Head, 2003; Grindrod and Hoogenboom, 2006). To date, no numerical model of nova formation has been developed, whereas numerical models of corona formation have predominantly focused on crustal surface flexure cased by mantle diapirs/plumes and/or lithospheric gravitational instabilities (e.g., Stofan et al., 1991; Janes et al., 1992; Koch, 1994; Koch and Manga, 1996; Smrekar and Stofan, 1997; Hoogenboom and Houseman, 2006; Elkins-Tanton et al., 2007; Stein et al., 2010). Whereas these models were able to reproduce some of the observed coronae topographies, predicted corona sizes were often larger (600–3000 km, Smrekar and Stofan, 1997; Hoogenboom and Houseman, 2006) than average 250 km diameter of Venus coronae (Smrekar et al., 2010). Recently, an alternative magmatic loading model (Dombard et al., 2007) demonstrated that crustal deformation caused by spreading of a giant melt intrusion in a ductile lower crust could possibly account for smaller (200–300 km) coronae sizes (Dombard et al., 2007).

Indeed, all previous numerical models of coronae were two-dimensional or assumed cylindrical geometry and characteristic surface fracturing patterns of novae and coronae were not reproduced due to rheological limitations. In addition, previous thermomechanical models assumed relatively strong and thick lithosphere (Smrekar and Stofan, 1997; Hoogenboom and Houseman, 2006). However, recent global mapping of crustal and lithospheric thickness on Venus suggest that 47% of the planet has an estimated very low elastic thickness value of 0–20 km, indicating either isostatic compensation or thin elastic lithosphere (Anderson and Smrekar, 2006). Thin elastic lithosphere of 10–20 km has also been detected under some of the recently volcanically active hotspots on Venus associated with mantle plumes (Smrekar et al., 2010). Most recent study of crustal thickness and support of topography on Venus (James et al., 2013) also used rather low globally-uniform elastic thickness of 20 km as a best-fit model parameter. These findings suggest that some of coronae and nova structures may actually result from mantle plumes/diapirs interaction with the thin and warm Venus lithosphere that may allow penetration of mantle upwellings to the bottom of the crust (e.g., Koch and Manga, 1996). This plausible scenario associated with strong decompression melting of the plume (e.g., Ueda et al., 2008; Sobolev et al., 2011) has not been modeled thermomechanically, thus leaving a gap in quantitative testing of potential mechanisms for novae and coronae formation.

This work documents results from new 3D numerical thermomechanical model of mantle plume/diapir interaction with a relatively warm and thin lithosphere having Venus-like surface temperature and gravity conditions (Fig. 1). The viscous-brittle/plastic rheological model is based on experimentally determined flow laws and allows for crustal fracturing, which can be compared to observations. The spontaneous development of both nova-like and corona-like structures with characteristic radial and concentric fracture patterns was systematically reproduced in numerical experiments.

2. Numerical model

The initial model setup impinges a thermal mantle plume/diapir (30–100 km in radius) into a thin and warm lithosphere with 35 km thick mafic crust (Fig. 1). Tail-free geometry of the plume is assumed in accordance with previous results suggesting dominance of discrete plume heads (thermals) on Venus (Jellinek et al., 2002). The Eulerian computational domain is equivalent to $404 \times 404 \times 100$ km^3 (Fig. 1) and is resolved with a regular rectangular grid of $405 \times 405 \times 101$ nodes and contains 130 millions randomly distributed Lagrangian markers (both smaller and larger models were also explored, see Table 1). All sides of the model have free slip mechanical boundary conditions. The free surface boundary condition atop the crust is implemented by using a "sticky" atmosphere (Schmeling et al., 2008) with low density (1 kg/m^3) and viscosity (10^{18} Pa s). The employed numerical code I3ELVIS (Gerya and Yuen, 2007) combines conservative finite differences on a fully staggered grid and marker-in-cell techniques with multigrid solver. This allows for large viscosity contrasts and strong localization of visco-brittle/plastic deformation (Gerya, 2010, 2013). The momentum, mass and heat conservation equations are solved on

Table 1
Conditions and results of numerical experiments.

Model	Model width (km)	Model height (km)	Grid step size (km)	C_0/C_1[a] (MPa)	ϕ_0[a]	Maximal viscosity (Pa s)	Plume width/height (km)	Plume temperature (K)	Mantle temperature (K)	Results
vean	196	100	1	10/3	0.1	10^{23}	80/40[b]	2060	1758	pre-nova dome, nova, corona
veap	202	98	0.5	1/1	0.1	10^{23}	80/40[b]	2060	1758	pre-nova dome, nova[e]
veas	196	100	1	1/1	0.1	10^{23}	80/40[b]	1960	1658	pre-nova dome, nova, corona
veat	196	100	1	1/1	0.1	10^{23}	90/45	1960	1658	pre-nova dome, nova, corona
vebk	500	100	1	20/3	0.15	10^{23}	90/45	1960	1658	pre-nova dome, nova, no corona (Fig. 6)
vebm	196	100	1	20/3	0.15	10^{23}	110/55	1973	1658	pre-nova dome, nova, no corona
vebn	196	100	1	1/1	0.1	10^{24}	90/45	1960	1658	pre-nova dome, nova, corona
vebo	196	100	1	1/1	0.1	10^{24}	100/40	1960	1658	pre-nova dome, nova, corona
vebp	404	100	1	1/1	0.1	10^{24}	100/40	1960	1658	pre-nova dome, nova, corona (Fig. 2)
vebpc[d]	404	100	1	1/1	0.1	10^{24}	100/40	1960	1658	pre-nova dome, nova, no corona
vebq	404	100	1	1/1	0.1	10^{24}	200/40	1960	1658	pre-nova dome with an outer rise, nova, corona (Fig. 4)
vebr	404	100	1	1/1	0.1	10^{24}	150/40	1960	1658	pre-nova plateau with an outer rise, nova with an outer rise, corona
vebs	404	100	1	1/1	0.1	10^{24}	80/40	1960	1658	pre-nova dome, nova, no corona
vebt	404	100	1	1/1	0.1	10^{24}	60/30	1960	1658	dome, no nova, no corona
vedc[d]	404	164	1	1/1	0.1	10^{24}	100/50[c]	1960	1658	pre-nova dome with an outer rise, nova with a central crater-like depression, corona (Fig. 7a)

[a] ϕ_0 is the internal friction coefficient, C_0 and C_1 are the initial and final rock strength, respectively.
[b] Equivalent values, spherical plume with 30 km radius was prescribed at the depth of 65 km.
[c] Equivalent values, spherical plume with 40 km radius was prescribed at the depth of 120 km.
[d] Diabase flow law (Ranalli, 1995) is used for the crust.
[e] Experiment has been stopped after nova formation.

the non-deforming Eulerian grid whereas the advection of transport properties including viscosity, plastic strain, temperature etc. is performed with the moving Lagrangian markers.

The initial thermal structure and thickness of the lithosphere (Fig. 1) is defined by a linear geotherm with 753 K at the surface and 1658–1758 K (Table 1) asthenospheric mantle temperature (Armann and Tackley, 2012) at 50 km depth. An adiabatic thermal gradient of 0.5 K/km is initially prescribed in the asthenospheric mantle. The simplified mantle plume is prescribed in the center of the model as a deep half-ellipsoid shaped mantle region with elevated (1960–2060 K, Table 1) temperature (Fig. 1). Temperature dependent thermal conductivity is used for the mantle $[k = 0.73 + 1293/(T + 77)]$ and the crust $[k = 1.18 + 474/(T + 77)]$ (Clauser and Huenges, 1995). The thermal boundary conditions are 753 K at the top, 1673 K (1773 K in hotter mantle models) at the bottom and zero heat flux on all other sides of the model. In order to insure an efficient heat transfer from the surface of the crust thermal conductivity of the "sticky" atmosphere (Fig. 1) is taken to be hundred times higher (200 W/m/K) than that of the lithosphere (1–4 W/m/K). Gravitational acceleration of 8.87 m/s^2 has been used in the model.

The rheological model implies constant low viscosity (10^{18} Pa s) of molten crust and magma extracted from the plume. State of the art visco-plastic rheology is used for the solid mafic crust and mantle based on experimentally determined flow laws (Ranalli, 1995): dry olivine flow law is used for the mantle and plagioclase (An_{75}) flow law is applied for the mafic crust (stronger diabase flow law has also been tested for the crust, Table 1). An upper cutoff limit of 10^{23}–10^{24} Pa s (Table 1) is used for the crustal and mantle viscosity that is high enough to ensure negligible viscous deformation of the brittle upper crust. State of the art brittle/plastic rheology of the crust assumes fracture-related strain weakening (Lavier et al., 2000; Huismans and Beaumont, 2002; Hieronymus, 2004; Buck et al., 2005; Choi et al., 2008; Gerya and Burg, 2007; Gerya, 2010, 2013) induced by percolation of magmatic fluids and is implemented by using rock strength limitation in form

$$\sigma_{II} \leqslant C_\gamma + \phi_\gamma P$$

$$\phi_\gamma = 1 \quad \text{when } P < 0 \quad \text{(tensile fracture)},$$

$$\phi_\gamma = \phi_0(1 - \gamma/\gamma_0) \quad \text{for } \gamma \leqslant \gamma_0 \text{ and } \phi_\gamma = 0 \text{ for } \gamma > \gamma_0 \text{ when } P \geqslant 0 \quad \text{(confined fracture)}$$

$$C_\gamma = C_0 + (C_1 - C_0)\gamma/\gamma_0 \quad \text{for } \gamma \leqslant \gamma_0 \text{ and } C_\gamma = C_1 \text{ for } \gamma > \gamma_0$$

$$\gamma = \int \sqrt{\frac{1}{2}(\dot{\varepsilon}_{ij(\text{plastic})})^2}\, dt,$$

$$\sigma_{II} = \sqrt{\frac{1}{2}\left(\sigma'_{ij}\right)^2},$$

where σ_{II} is second stress invariant (Pa), P is dynamic pressure on solids (Pa), ϕ_γ is the internal friction coefficient for the confined fractures (ϕ_0 is the initial internal friction coefficient), $\gamma \geqslant 0$ is integrated plastic strain ($\gamma_0 = 0.1$ is the upper strain limit for the fracture-related weakening caused by percolation of magmatic fluids; Gerya and Burg, 2007), t is time (s), $\dot{\varepsilon}_{ij(\text{plastic})}$ is plastic strain rate tensor, C_γ is the rock strength at $P = 0$ (for both confined and tensile fracture) that depends on the plastic strain γ (C_0 and C_1 are the initial and final strength values for the fracture-related weakening, respectively). The stress limitation for tensile fracture is formulated from a theoretical criterion (Rozhko et al., 2007) for tensile failure of a fluid-filled crack. This criterion is based on Griffith's theory (Murrell, 1964) and has been verified experimentally (Jaeger, 1963). Strain weakening assumed in the model is similar to those in previous numerical models of magma-assisted tectonic processes such as mid-ocean ridge extension (Hieronymus, 2004; Buck et al., 2005; Choi et al., 2008; Gerya, 2010, 2013) and intrusion emplacement into the crust (Gerya and Burg, 2007).

Partial melting of the mantle plume, melt extraction and percolation toward the bottom of the crust is implemented in a simplified manner (Gerya, 2013). According to our model, mafic magma added to the crust is balanced by melt production and extraction in the plume. However, melt percolation (e.g., Katz, 2010) is not modeled directly and considered to be nearly instantaneous (Connolly et al., 2009). The standard (i.e. without melt

extraction) volumetric degree of mantle melting M_0 changes with pressure and temperature according to the parameterized batch melting model of Katz et al. (2003). Lagrangian markers track the amount of melt extracted during the evolution of each experiment. The total amount of melt, M, for every marker takes into account the amount of previously extracted melt and is calculated as (Nikolaeva et al., 2008)

$$M = M_0 - \sum_n M_{\text{ext}},$$

where $\sum_n M_{\text{ext}}$ is the total melt fraction extracted during the previous n extraction episodes. At the initial moment of time (Fig. 1), all mantle and plume rocks are assumed to be melt-depleted ($\sum_n M_{\text{ext}} = M_0$). The rock is considered non-molten (refractory) when the extracted melt fraction is larger than the standard one (i.e. when $\sum_n M_{\text{ext}} > M_0$). If $M > 0$ for a given marker, the melt fraction $M_{\text{ext}} = M$ is extracted and $\sum_n M_{\text{ext}}$ is updated. The extracted melt fraction M_{ext} is assumed to propagate much faster than the rocks deform (Connolly et al., 2009). Melts produced in the entire model are added evenly to the top of the shallowest partially molten mantle region located atop the plume. The magma region forms atop the plume by accumulation of the extracted melts at the deforming crust/mantle boundary. Size and shape of the magma region forms spontaneously (Fig. 2a, right column) and is regulated by the dynamics of melt supply from the plume and lithospheric and crustal deformation. In this simplified model no flow field divergence is created in response to melt accretion to the bottom of the magma region. Additional space for the melt is assumed to be created by viscous compaction and subsidence of the melt-bearing mantle inside the plume. In order to ensure melt volume conservation and account for mantle compaction and subsidence in response to the melt extraction, melt addition to the bottom of the magma region is performed at every time step by converting the shallowest markers of hot partially molten mantle into new magma markers. The total volume of these new magma markers matches the total volume of extracted melt computed for the time step. This simple crust accretion algorithm does not account for volcanic processes and dyking above the magma regions, neither does it account for internal convection, melt segregation and crystal differentiation inside these regions.

Crystallization of magma and melting of the crust are computed from the simple linear batch melting model (Gerya, 2013)

$$M = 0 \quad \text{when } T < T_{\text{solidus}},$$

$$M = (T - T_{\text{solidus}})/(T_{\text{liquidus}} - T_{\text{solidus}})$$

$$\text{when } T_{\text{solidus}} < T < T_{\text{liquidus}},$$

$$M = 1 \quad \text{when } T > T_{\text{liquidus}},$$

where M is volumetric melt fraction, $T_{\text{solidus}} = 1327 + 0.091P$ and $T_{\text{liquidus}} = 1423 + 0.105P$ are, respectively, solidus and liquidus temperature (K) of the crust (Hess, 1989) at a given pressure P (MPa). The effective density of the mafic magma and molten crust is calculated as (Gerya, 2013)

$$\rho_{\text{eff}} = \rho_{\text{solid}}\left(1 - M + M\frac{\rho_{0\text{molten}}}{\rho_{0\text{solid}}}\right)$$

where $\rho_{0\text{solid}} = 3000$ kg/m^3 and $\rho_{0\text{molten}} = 2800$ kg/m^3 are the standard densities of solid and molten crust, respectively and ρ_{solid} is the density of solid crust at given P and T computed from

$$\rho_{\text{solid}} = \rho_{0\text{solid}} \times \big(1 - \alpha(T - 298)\big) \times \big(1 + \beta(P - 0.1)\big),$$

where $\alpha = 3 \times 10^{-5}$ 1/K and $\beta = 10^{-5}$ 1/MPa are thermal expansion and compressibility of the crust. The effect of latent heating due to equilibrium crystallization of molten rocks is included implicitly by increasing the effective heat capacity (Cp_{eff}) and the thermal expansion (α_{eff}) of the partially crystallized/molten rocks ($0 < M < 1$), calculated as (Gerya, 2013)

$$Cp_{\text{eff}} = Cp + Q_L\left(\frac{\partial M}{\partial T}\right)_{P=\text{const}},$$

$$\alpha_{\text{eff}} = \alpha + \rho\frac{Q_L}{T}\left(\frac{\partial M}{\partial P}\right)_{T=\text{const}},$$

where $Cp = 1000$ J/kg is the heat capacity of the solid crust and $Q_L = 380$ kJ/kg is the latent heat of crystallization of the crust (Turcotte and Schubert, 2002).

3. Numerical results

Reference model development (Fig. 2) shows six subsequent stages that differ in terms of crustal deformation and topography patterns: (1) pre-nova doming (Fig. 2a), (2) young (Fig. 2b) and (3) mature (Fig. 2c) nova stages, (4) advancing (Fig. 2d), (5) subsiding (Fig. 2e) and finally (6) fossil (Fig. 2f) corona stages. Pre-nova doming is characterized by the plume–lithosphere mechanical interaction producing surface uplift and by the decompression melting of the plume, which gives rise to the emplacement of a large lower-crustal intrusion. A broad topographic dome forms at the surface, which is dissected by radial and concentric fractures. Some concentric fractures also form at the outer margins of the dome (Fig. 2a). Young and mature nova stages associate with intense lower crustal melting, triggered by heat and magma from the plume (Fig. 2b, c). Buoyancy of molten rocks initiates a localized crustal convection cell, which pierces the crust (Fig. 2c). The rise of the convection cell is manifested by focused surface uplift at the center of the pre-nova dome, thus forming a young steep-sided nova rise (Fig. 2a–c, Fig. 3, 0.3–3.3 Myr). At the mature nova stage, a weakly-pronounced wide circular depression and outer rise start to form around the nova rise (Fig. 2c, Fig. 3, 3.3 Myr). The nova rise is intensely dissected by a characteristic stellate pattern of radial tensile fractures (Crumpler et al., 1996) (Fig. 2b, c), which can serve for the development of dike swarms (e.g., Grosfils and Head 1995, 1996; Ernst et al., 2001). Small transient crater-like central depression can also form in some models (model “vedc” in Table 1), due to the strong concentric tensile crustal deformation atop the rising nova. At the mature nova stage, molten rocks close to the surface may cause massive volcanism, which is also documented for some of the nova rises (Krassilnikov and Head, 2003).

If the buoyant force of the partially molten crustal convection cell overcomes the brittle strength of the upper crustal lid, the mature nova structure can be transformed into an advancing corona (Fig. 2d). This happens by concentric inward-dipping fracturing of the nova rise margins and subsequent overthrusting of partially molten lower-middle crustal rocks over the surface of the down-bending brittle upper crust. An annuli fracture pattern forms at this stage (Fig. 2d). An outer annulus of concentric normal faults forms in the extensional outer rise region of the downbending upper crust, similar to terrestrial outer rise bending regions of subducting oceanic slabs (Ranero et al., 2003). An inner annulus is comprised of inward dipping concentric thrust faults marking the advancing front of the overriding crustal wedge supplied by partially molten crust spreading outward. Between these two contrasting tectonic regions a deep trench-like depression forms (Fig. 2d), which is again similar to the situation in subduction zones. The process thus resembles retreating subduction (e.g., Sandwell and Schubert, 1992; Ueda et al., 2008) at its incipient stage. The overthrusted rudimentary concentric upper-crustal slab warms up rapidly and recycles into the convection cell. The advancing corona reaches its maximal lateral extent within the

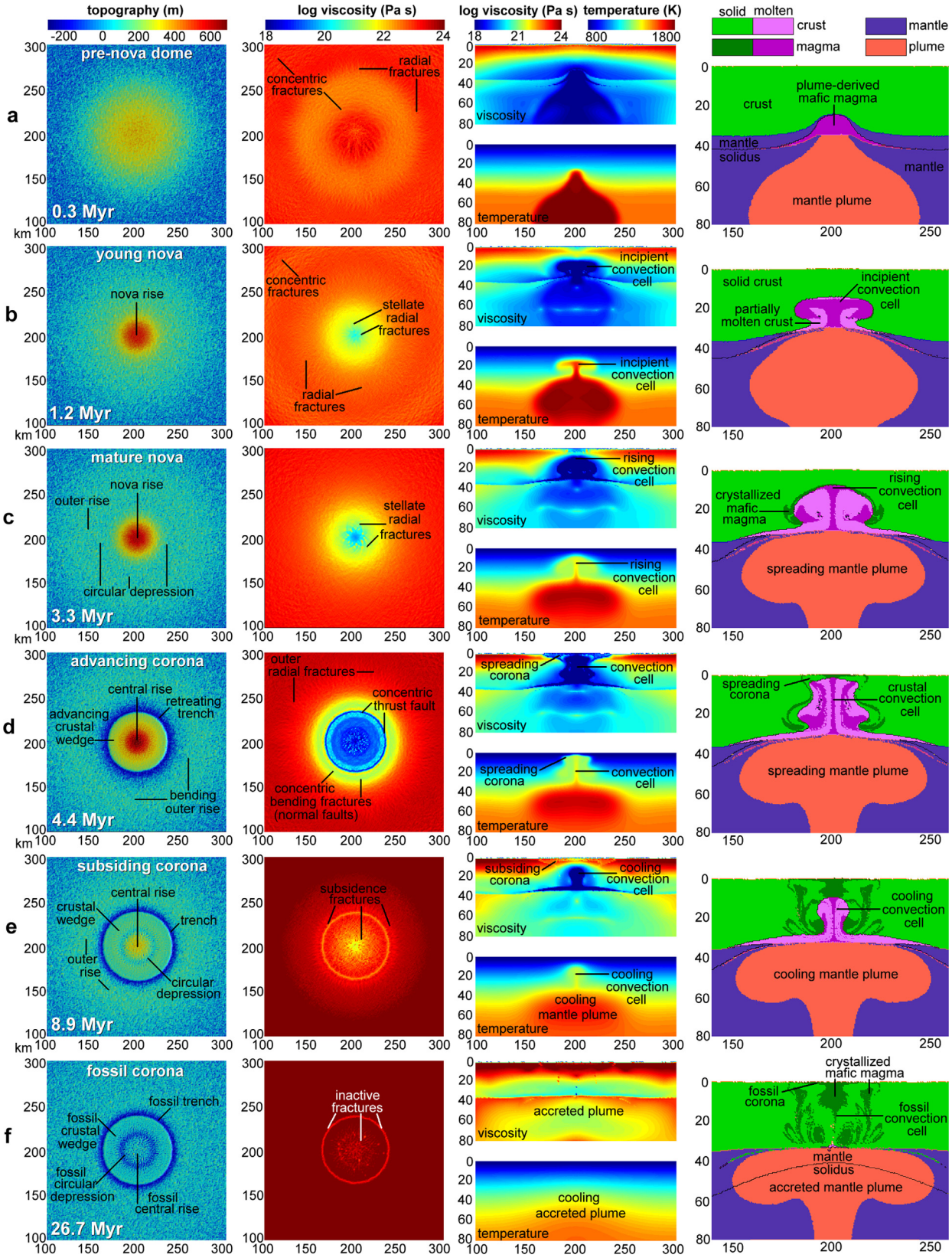

Fig. 2. Subsequent development of the nova and corona structures in the reference numerical model (model "vebp" in Table 1). Topography in the first column is computed relative to the level of 10 km from the top of the model. Distribution of the effective viscosity of the crust ($\eta_{\text{eff}} = \frac{\sigma_{II}}{2\dot{\varepsilon}_{II}}$, where $\sigma_{II} = \sqrt{\frac{1}{2}(\sigma'_{ij})^2}$ and $\dot{\varepsilon}_{II} = \sqrt{\frac{1}{2}(\dot{\varepsilon}_{ij})^2}$ are second invariants of deviatoric stress and strain rate, respectively) in the second column is taken at the topographic surface. Distribution of the effective viscosity takes into account localized brittle deformation and shows patterns of the active fractures at the surface.

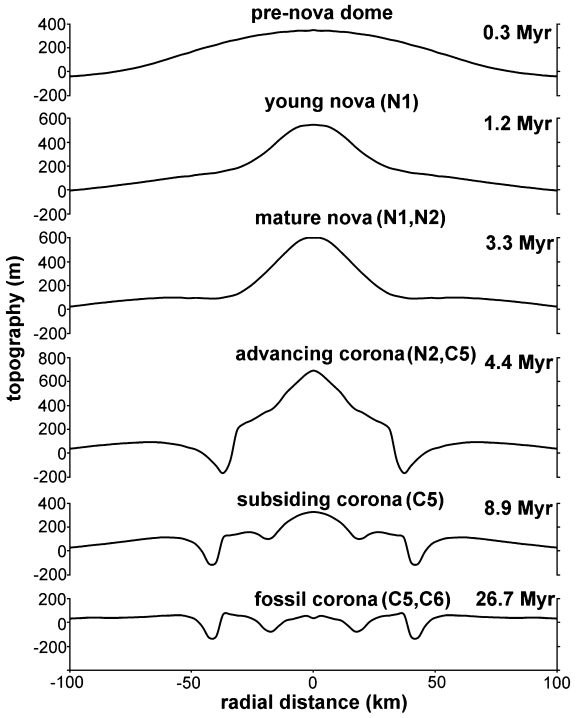

Fig. 3. Modeled radial topography profiles for different stages of the reference model development shown in Fig. 2. Numbers in brackets refer to possible topographic groups of nova and coronae discussed in the text.

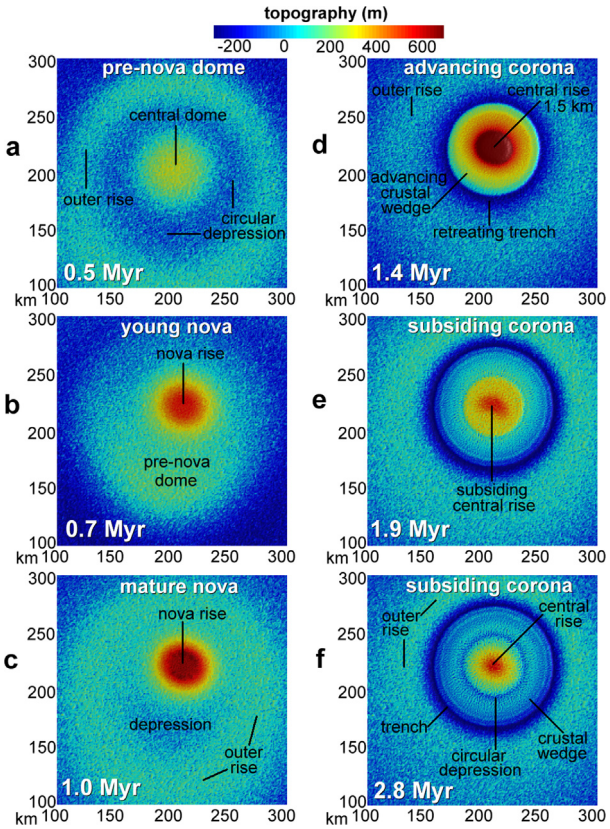

Fig. 4. Topography evolution for the model with large and wide plume (model "vebq" in Table 1). Note that nova and corona are displaced relative to the center of the plume.

next 1–2 Myr and then begins subsiding in response to the conductive cooling of the crustal convection cell at the surface and the surrounding colder crust (Fig. 2e). Cooling leads to the gradual solidification of partially molten rocks, which lasts for more than 15 Myr (Fig. 2e, f, right column). The longevity of the crustal convection cell is related to the heat supply from the gradually spreading and cooling mantle plume that finally becomes accreted to the lithosphere (Fig. 2e, f). Surface development during the subsidence stage is manifested in an overall topographic relaxation associated with a preferential degradation of the central rise high (Fig. 2e, Fig. 3, 8.9 Myr). An inner circular depression separating the rise and the crustal wedge forms at this stage (Fig. 2e, Fig. 3, 8.9 Myr). The active fracture pattern during this stage differs significantly from the advancing corona and consists of weakly pronounced radial fractures, which dissect both the inner and outer zones of the corona (Fig. 2e). At the culminate stage of the process (Fig. 2f) the crustal convection cell becomes inactive due to the complete solidification of previously molten crustal rocks. A flat topography forms (Fig. 2f, Fig. 3, 26.7 Myr), which preserves the zoning of the subsiding corona pattern. In the end a fossilized corona forms, which continues to exist as a tectonically inactive, yet visible surface feature (Fig. 2f, left column).

It is also worth noting that, despite of magma addition to the crust, the reference model development associates with overall crustal thinning under nova and corona structures (Fig. 2, right column). This crustal thinning results from the strong lithospheric extension above the spreading plume head (Fig. 2a–d, right column) and relaxes partly during the subsiding and fossil corona stages (Fig. 2e, f, right column).

4. Influence of model parameters

The corona size depends directly on the size of the mantle plume/diapir. Large plumes release more magma and heat into the lower crust and produce bigger coronae, which also develop more rapidly (cf. Fig. 2 and Fig. 4). Further, larger and wide plumes tend to produce a complex topography during the pre-nova doming: the central dome is surrounded by a circular depression and an outer rise (Fig. 4a). The shape of the initial magma region formed in the crust can change from dome-shaped (Fig. 2a, right column) to ring-shaped (Fig. 5a): rapid spreading of the large and wide plume may produce a ring-like deflection of the crust/mantle boundary, where magma derived from the plume accumulates. A molten crustal convection cell develops asymmetrically from this ring and the resulting corona and nova structures are displaced relative to the center of the plume (Fig. 4). The ring-like magma regions above very large and wide plumes may potentially trigger multiple crustal convection cells, which can form related coronae at the surface (Fig. 5). On the other hand, smaller plumes/diapirs fail to form corona (model "vebs" in Table 1) and produce only nova structures. In these models, a smaller crustal convection cell is located at the bottom of the crust and fails to pierce through the brittle upper crust. A similar development is characteristic for the model with a crust of greater brittle and/or ductile strength (Fig. 6, models "vebk", "vebm" and "vebpc" in Table 1). Although the crustal convection cell in these models has a usual size (i.e. as in Fig. 2c, right column) it is unable to pierce through the stronger upper crust and fails to form a corona.

5. Discussion and conclusions

Numerical topographic and fracture patterns show notable similarities with some small to moderate size novae and coronae on Venus (Figs. 3, 7). In particular, some of the observed topographic groups of novae and coronae spontaneously form in our experiments (cf. Fig. 3). The topography rise associated with the stellate fracture pattern resembles some of the typical nova structures observed on Venus (Fig. 7a, c) (Krassilnikov and Head, 2003). Stellate

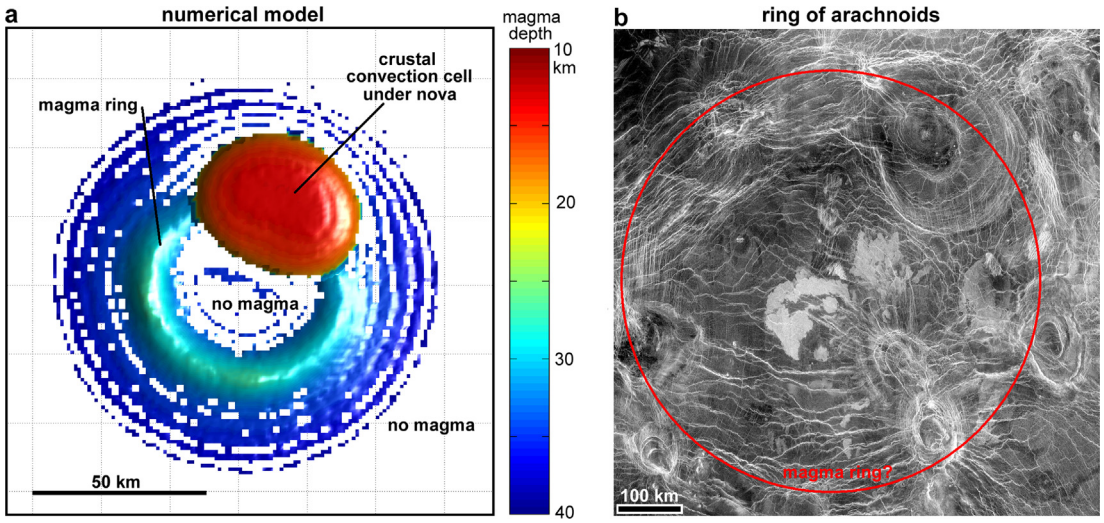

Fig. 5. Ring-like magma distribution above the large and wide mantle plume for the mature nova stage (a) (Fig. 4c) compared with ring-like distribution of arachnoids on Venus (b) (http://pds.jpl.nasa.gov/planets/captions/venus/arach.htm). The circle in (b) shows presumable position of a lower-crustal magma ring formed by a large and wide mantle plume, which possibly produced the arachnoids. Note that spatial scales of (a) and (b) are different.

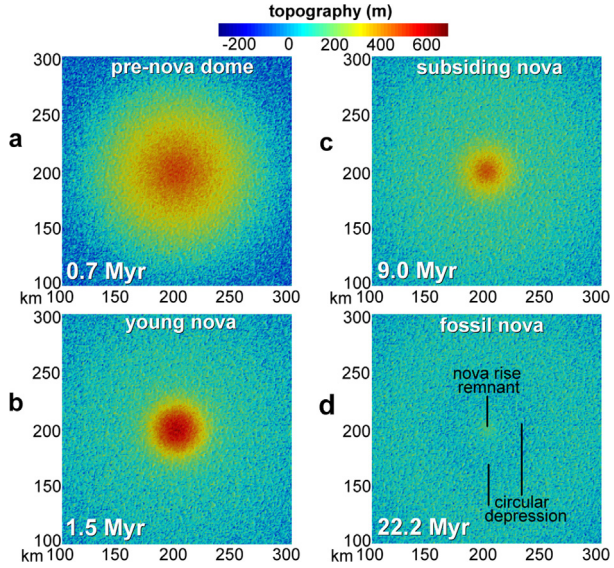

Fig. 6. Topography evolution for the model with strong brittle crust (model "vebk" in Table 1). No corona is formed in this model.

pattern of tensile fractures obtained for novae structures often associate with crater-like central depression observed in many natural raised novae (Fig. 7a, c). Complex modeled corona patterns also find analogies in nature (Figs. 3, 7b, d, 8). In particular, the multiple annuli structure of the Aramaiti Corona, which has not been reproduced in previous numerical models, compares well with the subsiding corona structure (Fig. 7b, d), in which five zones can be distinguished: central rise, circular depression, crustal wedge with thrust faults, circular trench, and outer rise with normal faults. It should be mentioned, however, that the size of the numerical corona for the reference model is 2.5–3 times smaller than the actual size of the Aramaiti Corona, which was presumably produced by a ca. 3 times larger mantle plume/diapir than explored in the reference model. The lack of a pronounced central depression in numerical coronae may in part be due to the simplified incompressible model, which does not account for significant thermal contraction during crystallization of molten rocks under the corona (Fig. 2c–f, right column). Future model improvement could also include addition of elasticity and parameterizations for the surface volcanism and dike swarm emplacement. Subsequent work could also focus on modeling gravity signatures of novae and coronae produced by modifications of Venus surface topography as well as underlying crustal and mantle density structures (e.g., Schubert et al., 1994). In particular, crustal thinning above the spreading plume found in our numerical experiments (Fig. 2, right column) could be partly responsible for positive gravity anomalies associated with some coronae (e.g., Schubert et al., 1994).

Crustal convection mechanism of novae and coronae formation requires thin and warm lithosphere with weak ductile crust, which enables large horizontal surface displacements (outward thrusting). This thrusting correlates with some of the observed nova and coronae structures (Figs. 7d, 8) and is in strong contrast with predominantly vertical surface motions predicted by previous thermomechanical coronae models with strong rigid lithosphere (Smrekar and Stofan, 1997; Hoogenboom and Houseman, 2006; Elkins-Tanton et al., 2007). Warm lithosphere allows to reproduce successfully characteristic stellate novae structures and model observed transformation of some novae to coronae (Krassilnikov and Head, 2003). Warm lithosphere assumption seems also to be in agreement with previous suggestion (Krassilnikov and Head, 2003) that vanishing of coronae activity after regional plains formation may be due to thickening of the lithosphere with time (Krassilnikov and Head, 2003). However, numerical novae and coronae do not comprise the entire spectrum of observed sizes and topographic groups of these structures (Krassilnikov and Head, 2003; Smrekar and Stofan, 1997). Therefore, plume-induced crustal convection is advocated here as a plausible but non-unique mechanism of novae and coronae formation on Venus.

One important question concerns the thermomechanical reasons for the apparent absence of novae and coronae on Earth, although they have similarities with some terrestrial features associated with large-scale magmatism and giant dike swarms (Herrick, 1999; Lopez et al., 1999; Ernst et al., 2001). A possible explanation is the high surface temperature on Venus compared to Earth. The numerical models suggest the critical condition for the documented novae and coronae development is a low-viscosity ductile crust with a hot and thin brittle upper crustal layer. The relatively low strength of this thin upper layer can be easily overcome by the buoyancy of large volumes of plume-induced magmas emplaced into the ductile lower crust. Consequently, instead of forming large flattened intrusions in the lower crust (Dombard et al., 2007) these magmas can rise as partially molten crustal convection cells. These convection cells can pierce and fracture the thin brittle upper

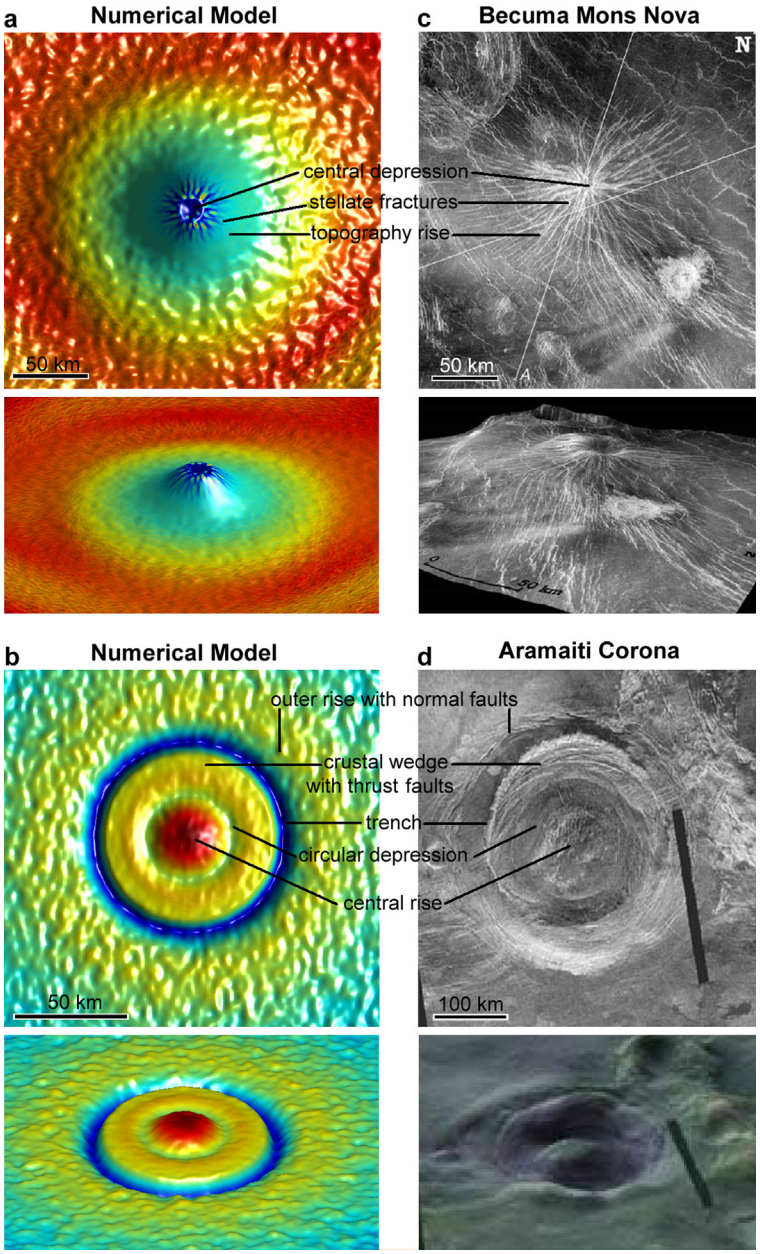

Fig. 7. Comparison of the simulated nova (a) (model "vedc" at 4.0 Myr, Table 1) and corona (b) (model "vebp" at 8.9 Myr, Fig. 2e, Table 1) patterns with the radar image (top) and topography projection (bottom) of the Becuma Mons nova (c) (Krassilnikov and Head, 2003) and Aramati Corona (d) (Grindrod and Hoogenboom, 2006). Color code in (a) and (b) is taken for the effective viscosity and topography, respectively. Note that spatial scales of (b) and (d) are different.

crust, thus forming various novae and coronae features at the surface. The hot surface temperature also precludes intense cooling of molten crustal rocks approaching the surface, this allows them to remain magmatically and tectonically active on a timescale of millions to tens of millions years, which is needed to form novae and coronae (Fig. 2).

The numerical results can also have some implications for the temporal relationship between novae and coronae on Venus. In the numerical experiments, the formation of corona destroys the smaller pre-existing (parent) nova rise (Figs. 2, 4). This may explain to some extent why on Venus novae are less common and (typically) smaller and younger than coronae (Krassilnikov and Head, 2003). This age and size discrepancy between novae and coronae can also be explained by the gradual cooling of the lithosphere and reduction of plume sizes with geological time (Krassilnikov and Head, 2003). Before the formation of regional planes on the surface of Venus, larger mantle plumes/diapirs triggered by a global resurfacing event (Strom et al., 1994; Armann and Tackley, 2012) interacted with warm and thin lithosphere producing many coronae that destroyed their parent nova structures (Figs. 2, 4). At the later stage, smaller mantle plumes became more common, interacting with colder and thicker lithosphere, preferentially producing novae rather than coronae (Table 1, Fig. 6). The models also suggest raised novae with a stellate fracture pattern (Figs. 2b–e, 3a, 6, 7a) are relatively short-living transient structures, which can be active today. These structures should be characterized by ongoing tectonic and magmatic activity and elevated heat emission (Smrekar et al., 2010) resulting from hot partially molten crustal rocks close to the surface.

Acknowledgements

S. Chapman, G. Golabek and J.-P. Burg are thanked for discussions and comments. Constructive comments and suggestions from

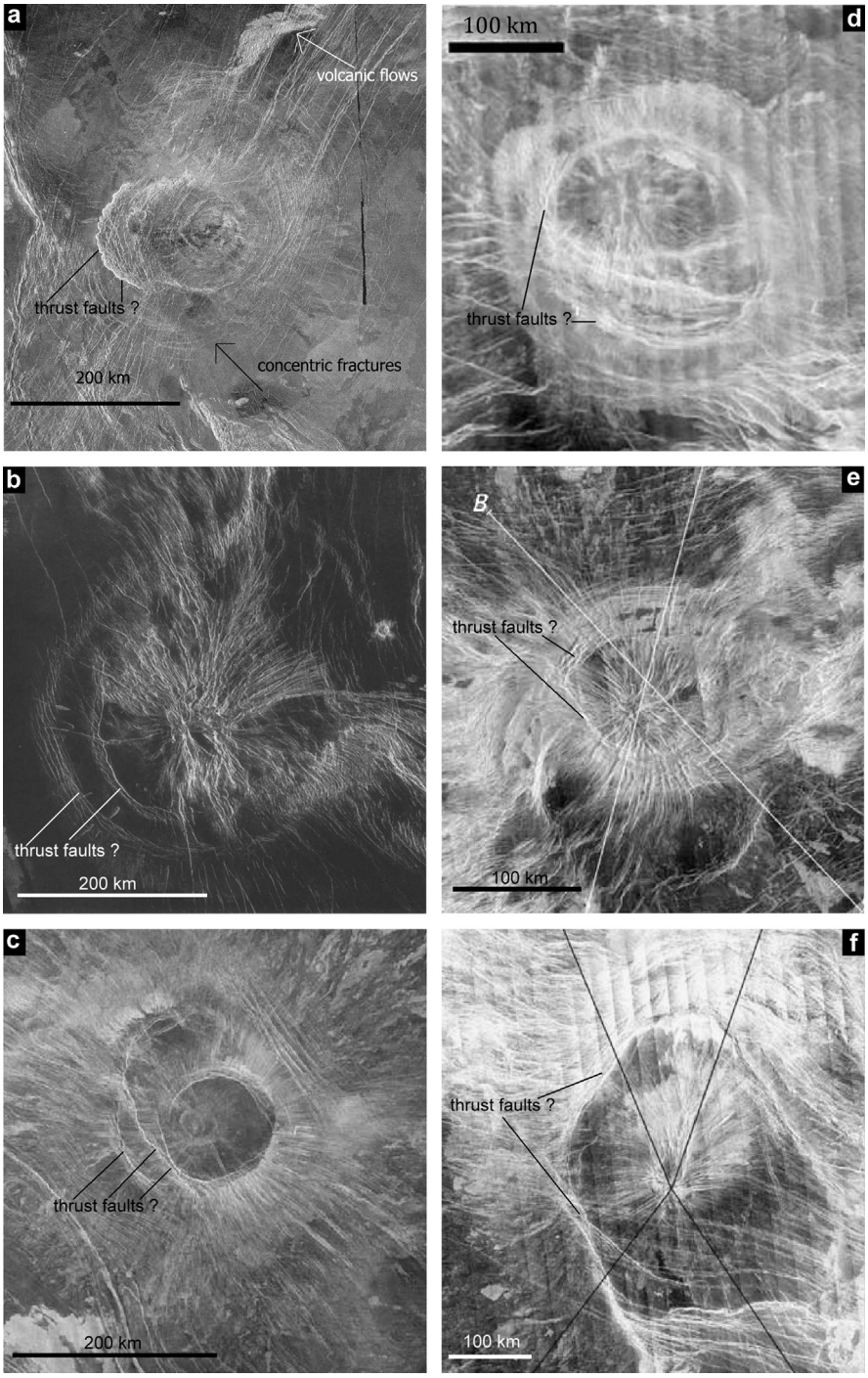

Fig. 8. Possible examples of inward dipping circular thrust faults formed by outward thrusting during novae and coronae formation. (a) Nalwomga Corona (Hoogenboom and Houseman, 2006). (b) Selu Corona (Janes et al., 1992). (c) Nagavonyi Corona (Grindrod and Hoogenboom, 2006). (d) Corona centered at 11.5°N latitude, 244°W longitude (Glaze et al., 2002). (e) Oduduwa Corona (nova) (Krassilnikov and Head, 2003). (f) Maram Corona (nova) (Krassilnikov and Head, 2003).

two anonymous reviewers are greatly appreciated. This work was supported by Crystal2Plate project of European Research Council and 4D-Adamello project of Swiss National Science Foundation.

References

Aittola, M., Kostama, V.-P., 2000. Venusian novae and arachnoids: characteristics, differences and the effect of the geological environment. Planet. Space Sci. 48, 1479–1489.

Anderson, F.S., Smrekar, S.E., 2006. Global mapping of crustal and lithospheric thickness on Venus. J. Geophys. Res. 111, E08006.

Armann, M., Tackley, P.J., 2012. Simulating the thermo-chemical magmatic and tectonic evolution of Venus' mantle and lithosphere 1. Two-dimensional models. J. Geophys. Res. 117, E12003.

Barsukov, V.L., Basilevsky, A.T., Kuzmin, R.O., Pronin, A.A., Nikolaeva, O.N., Chernaya, I.M., Burba, G.A., Bobina, N.N., Shashkina, V.P., Markov, M.S., Sukhanov, A.L., 1984. Preliminary evidence on the geology of Venus from radar measurements by the Venera 15 and 16 probes. Geokhimia 12, 1811–1820.

Basilevsky, A.T., Head, J.W., 1998. Onset time and duration of corona activity on Venus: Stratigraphy and history from photogeologic study of stereo images. Earth Moon Planets 76, 67–115.

Buck, W.R., Lavier, L.L., Poliakov, A.N.B., 2005. Modes of faulting at mid-ocean ridges. Nature 434, 719–723.

Choi, E., Lavier, L., Gurnis, M., 2008. Thermomechanics of mid-ocean ridge segmentation. Phys. Earth Planet. Inter. 171, 374–386.

Clauser, C., Huenges, E., 1995. Thermal conductivity of rocks and minerals. In: Ahrens, T.J. (Ed.), Rock Physics and Phase Relations. In: AGU Reference Shelf, vol. 3. American Geophysical Union, Washington, DC, pp. 105–126.
Connolly, J.A.D., Schmidt, M.W., Solferino, G., Bagdassarov, N., 2009. Permeability of asthenospheric mantle and melt extraction rates at mid-ocean ridges. Nature 462, 209–212.
Crumpler, C.S., Aubele, J.C., Head, J.W., 1996. Venus volcanic feature catalogue. http://porter.geo.brown.edu/planetary/databases.html.
Dombard, A.J., Johnson, C.L., Richards, M.A., Solomon, S.C., 2007. A magmatic loading model for coronae on Venus. J. Geophys. Res. 112, E04006.
Elkins-Tanton, L.T., Smrekar, S.E., Hess, C., Parmentier, E.M., 2007. Volcanism and volatile recycling on a one-plate planet: Applications to Venus. J. Geophys. Res. 112, E04S06.
Ernst, R.E., Grosfils, E.B., Mége, D., 2001. Giant dike swarms: Earth, Venus, and Mars. Annu. Rev. Earth Planet. Sci. 29, 489–534.
Gerya, T., 2010. Dynamical instability produces transform faults at mid-ocean ridges. Science 329, 1047–1050.
Gerya, T.V., 2013. Three-dimensional thermomechanical modeling of oceanic spreading initiation and evolution. Phys. Earth Planet. Inter. 214, 35–52.
Gerya, T.V., Yuen, D.A., 2007. Robust characteristic method for modeling multiphase visco-elasto-plastic thermo-mechanical problems. Phys. Earth Planet. Inter. 163, 83–105.
Gerya, T.V., Burg, J.-P., 2007. Intrusion of ultramafic magmatic bodies into the continental crust: Numerical simulation. Phys. Earth Planet. Inter. 160, 124–142.
Glaze, L.S., Stofan, E.R., Smrekar, S.E., Baloga, S.M., 2002. Insights into corona formation through statistical analyses. J. Geophys. Res. 107, 5135.
Grindrod, P.M., Hoogenboom, T., 2006. Venus: The corona conundrum. Astron. Geophys. 47 (3), 16–21.
Grosfils, E.B., Head, J.W., 1995. Radiating dike swarms on Venus: Evidence for emplacement at zones of neutral buoyancy. Planet. Space Sci. 43, 1555.
Grosfils, E.B., Head, J.W., 1996. The timing of giant radiating dike swarm emplacement on Venus: Implications for resurfacing of the planet and its subsequent evolution. J. Geophys. Res. 101, 4645–4656.
Herrick, R.R., 1999. Small mantle upwellings are pervasive on Venus and Earth. Geophys. Res. Lett. 26, 803–806.
Hess, P.C., 1989. Origin of Igneous Rocks. Harvard University Press, London, UK.
Hieronymus, C.F., 2004. Control on seafloor spreading geometries by stress- and strain-induced lithospheric weakening. Earth Planet. Sci. Lett. 222, 177–189.
Hoogenboom, T., Houseman, G.A., 2006. Rayleigh–Taylor instability as a mechanism for corona formation on Venus. Icarus 180, 292–307.
Huismans, R.S., Beaumont, C., 2002. Asymmetric lithospheric extension: The role of frictional plastic strain softening inferred from numerical experiments. Geology 30, 211–214.
Ivanov, M.A., Head, J.W., 2001. Geology of Venus: Mapping of a global geotraverse at 30°N latitude. J. Geophys. Res. 106, 17,515–17,566.
Jaeger, J.C., 1963. Extension failures in rocks subject to fluid pressure. J. Geophys. Res. 68, 6066.
James, P.B., Zuber, M.T., Phillips, R.J., 2013. Crustal thickness and support of topography on Venus. J. Geophys. Res. 118, 859–875.
Janes, D.M., Turtle, E.P., 1996. Gravity signatures of corona precursors on Venus: Reality vs. prediction. Lunar Planet. Sci. XXVII, 605–606.
Janes, D.M., Squyres, S.W., Bindschsdler, D.L., Baer, G., Schubert, G., Sharpton, V.L., Stofan, H.E., 1992. Geophysical models for the formation and evolution of coronae on Venus. J. Geophys. Res. 97, 16,055–16,067.
Jellinek, A.M., Lenardic, A., Manga, M., 2002. The influence of interior mantle temperature on the structure of plumes: Heads for Venus, tails for the Earth. Geophys. Res. Lett. 29, 1532. http://dx.doi.org/10.1029/2001GL014624.
Katz, R.F., 2010. Porosity-driven convection and asymmetry beneath mid-ocean ridges. Geochem. Geophys. Geosyst. 11, Q0AC07.
Katz, R.F., Spiegelman, M., Langmuir, C.H., 2003. A new parameterization of hydrous mantle melting. Geochem. Geophys. Geosyst. 4, 1073.
Koch, D.M., 1994. A spreading drop model for plumes on Venus. J. Geophys. Res. 99, 2035–2052.
Koch, D.M., Manga, M., 1996. Neutral buoyant diapirs: A model for Venus coronae. Geophys. Res. Lett. 99, 225–228.
Krassilnikov, A.S., Head, J.W., 2003. Novae on Venus: Geology, classification, and evolution. J. Geophys. Res. 108, E9.
Lavier, L.L., Buck, W.R., Poliakov, A.N.B., 2000. Factors controlling normal fault offset in an ideal brittle layer. J. Geophys. Res. 105, 23431–23442.
Lopez, I., Marquez, A., Oyarzun, R., 1999. Are coronae restricted to Venus?: Corona-like tectonovolcanic structures on Earth. Earth Moon Planets 77, 125–137.
Murrell, S.A.F., 1964. The theory of propagation of elliptical Griffith cracks under various conditions of plane strain or plain stress. Parts 2, 3. Br. J. Appl. Phys. 15, 1123.
Nikolaeva, K., Gerya, T.V., Connolly, J.A.D., 2008. Numerical modelling of crustal growth in intraoceanic volcanic arcs. Phys. Earth Planet. Inter. 171, 336–356.
Ranalli, G., 1995. Rheology of the Earth. Chapman & Hall, London, UK.
Ranero, C.R., Phipps Morgan, J., Reichert, C., 2003. Bending-related faulting and mantle serpentinization at the Middle America trench. Nature 425, 367–373.
Roberts, K.M., Head, J.W., 1993. Large-scale volcanism associated with coronae on Venus: Implications for formation and evolution. Geophys. Res. Lett. 20, 1111–1114.
Rozhko, A.Y., Podladchikov, Y.Y., Renard, F., 2007. Failure patterns caused by localized rise in pore-fluid overpressure and effective strength of rocks. Geophys. Res. Lett. 34, L22304.
Sandwell, D.T., Schubert, G., 1992. Evidence for retrograde lithospheric subduction on Venus. Science 257, 766–770.
Schubert, G., Moore, W.B., Sandwell, D.T., 1994. Gravity over coronae and chasmata on Venus. Icarus 112, 130–146.
Schmeling, H., Babeyko, A.Y., Enns, A., Faccenna, C., Funiciello, F., Gerya, T., Golabek, G.J., Grigull, S., Kaus, B.J.P., Morra, G., Schmalholz, S.M., van Hunen, J., 2008. Benchmark comparison of spontaneous subduction models – Towards a free surface. Phys. Earth Planet. Inter. 171, 198–223.
Smrekar, S.E., Stofan, E.R., 1997. Corona formation and heat loss on Venus by coupled upwelling and delamination. Science 277, 1289–1294.
Smrekar, S.E., Stofan, E.R., Mueller, N., Treiman, A., Elkins-Tanton, L., Helbert, J., Piccioni, G., Drossart, P., 2010. Recent hotspot volcanism on Venus from VIRTIS emissivity data. Science 328, 605–608.
Sobolev, S.V., Sobolev, A.V., Kuzmin, D.V., Krivolutskaya, N.A., Petrunin, A.G., Arndt, N.T., Radko, V.A., Vasiliev, Y.R., 2011. Linking mantle plumes, large igneous provinces and environmental catastrophes. Nature 477, 312-U80.
Squyres, S.W., Janes, D.M., Baer, G., Bindschadler, D.L., Schubert, G., Sharpton, V.L., Stofan, E.R., 1992. The morphology and evolution of coronae on Venus. J. Geophys. Res. 97, 13611–13634.
Stein, C., Fahl, A., Hansen, U., 2010. Resurfacing events on Venus: Implications on plume dynamics and surface topography. Geophys. Res. Lett. 37, L01201.
Stofan, E.R., Bindschadler, D.L., Head, J.W., Parmentier, E.M., 1991. Corona structures on Venus: Models of origin. J. Geophys. Res. 96, 20,933–20,946.
Stofan, E.R., Smrekar, S.E., Tapper, S.W., Guest, J.E., Grindrod, P.M., 2001. Preliminary analysis of an expanded corona database for Venus. Geophys. Res. Lett. 28, 4267–4270.
Stofan, E.R., Sharpton, V.L., Schubert, G., Baer, G.D., Bindschadler, D.L., Janes, D.M., Squyres, S.W., 1992. Global distribution and characteristics of coronae and related features on Venus: Implications for origin and relation to mantle processes. J. Geophys. Res. 97, 13347–13378.
Strom, R.G., Schaber, G.G., Dawson, D.D., 1994. The global resurfacing of Venus. J. Geophys. Res. 99, 10,899–10,926.
Turcotte, D.L., Schubert, G., 2002. Geodynamics. Cambridge University Press, Cambridge, UK.
Ueda, K., Gerya, T., Sobolev, S.V., 2008. Subduction initiation by thermal–chemical plumes. Phys. Earth Planet. Inter. 171, 296–312.